

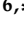







Article

Spectroelectrochemical Properties and Catalytic Activity in Cyclohexane Oxidation of the Hybrid Zr/Hf-Phthalocyaninate-Capped Nickel(II) and Iron(II) tris-Pyridineoximates and Their Precursors

Yan Z. Voloshin ^{1,2}, Semyon V. Dudkin ¹, Svetlana A. Belova ¹, Daniel Gherca ³, Dumitru Samohvalov ³ , Corina-Mihaela Manta ³, Maria-Andreea Lungu ³, Samuel M. Meier-Menches ⁴ , Peter Rapta ^{5,*} , Denisa Darvasiova ⁵ , Michal Malček ⁵ , Armando J. L. Pombeiro ⁶ , Luísa M. D. R. S. Martins ^{6,*}  and Vladimir B. Arion ^{7,*} 

- ¹ Nesmeyanov Institute of Organoelement Compounds of the Russian Academy of Sciences, 119991 Moscow, Russia; voloshin@ineos.ac.ru (Y.Z.V.); sdudkin@ineos.ac.ru (S.V.D.); savkinasveta91@mail.ru (S.A.B.)
- ² Department of General and Inorganic Chemistry, Gubkin Russian State University of Oil and Gas (National Research University), 119991 Moscow, Russia
- ³ Sara Pharm Solutions S.R.L., 266-268 Calea Rahovei, 050912 Bucharest, Romania; daniel_gherca@yahoo.com (D.G.); dumitru.samohvalov@sara-pharm.com (D.S.); corina.manta@sara-pharm.com (C.-M.M.); maria-andreea.lungu@sara-pharm.com (M.-A.L.)
- ⁴ Department of Analytical Chemistry, University of Vienna, Währinger Strasse 38, A-1090 Vienna, Austria; samuel.meier@univie.ac.at
- ⁵ Institute of Physical Chemistry and Chemical Physics, Faculty of Chemical and Food Technology, Slovak University of Technology in Bratislava, Radlinského 9, SK-812 37 Bratislava, Slovakia; denisa.darvasiova@stuba.sk (D.D.); michal.malcek@stuba.sk (M.M.)
- ⁶ Centro de Química Estrutural, Instituto Superior Técnico, Universidade de Lisboa, Av. Rovisco Pais, 1049-001 Lisboa, Portugal; pombeiro@tecnico.ulisboa.pt
- ⁷ Institute of Inorganic Chemistry, University of Vienna, Währinger Strasse 42, A-1090 Vienna, Austria
- * Correspondence: peter.rapta@stuba.sk (P.R.); luisammartins@tecnico.ulisboa.pt (L.M.D.R.S.M.); vladimir.arion@univie.ac.at (V.B.A.)



Citation: Voloshin, Y.Z.; Dudkin, S.V.; Belova, S.A.; Gherca, D.; Samohvalov, D.; Manta, C.-M.; Lungu, M.-A.; Meier-Menches, S.M.; Rapta, P.; Darvasiova, D.; et al. Spectroelectrochemical Properties and Catalytic Activity in Cyclohexane Oxidation of the Hybrid Zr/Hf-Phthalocyaninate-Capped Nickel(II) and Iron(II) tris-Pyridineoximates and Their Precursors. *Molecules* **2021**, *26*, 336. <https://doi.org/10.3390/molecules26020336>

Academic Editor:
Nikolay Gerasimchuk
Received: 13 December 2020
Accepted: 4 January 2021
Published: 11 January 2021

Publisher's Note: MDPI stays neutral with regard to jurisdictional claims in published maps and institutional affiliations.



Copyright: © 2021 by the authors. Licensee MDPI, Basel, Switzerland. This article is an open access article distributed under the terms and conditions of the Creative Commons Attribution (CC BY) license (<https://creativecommons.org/licenses/by/4.0/>).

Abstract: The in situ spectroelectrochemical cyclic voltammetric studies of the antimony-monocapped nickel(II) and iron(II) tris-pyridineoximates with a labile triethylantimony cross-linking group and Zr(IV)/Hf(IV) phthalocyaninate complexes were performed in order to understand the nature of the redox events in the molecules of heterodinuclear zirconium(IV) and hafnium(IV) phthalocyaninate-capped derivatives. Electronic structures of their 1e-oxidized and 1e-electron-reduced forms were experimentally studied by electron paramagnetic resonance (EPR) spectroscopy and UV–vis–near-IR spectroelectrochemical experiments and supported by density functional theory (DFT) calculations. The investigated hybrid molecular systems that combine a transition metal (pseudo)clathrochelate and a Zr/Hf-phthalocyaninate moiety exhibit quite rich redox activity both in the cathodic and in the anodic region. These binuclear compounds and their precursors were tested as potential catalysts in oxidation reactions of cyclohexane and the results are discussed.

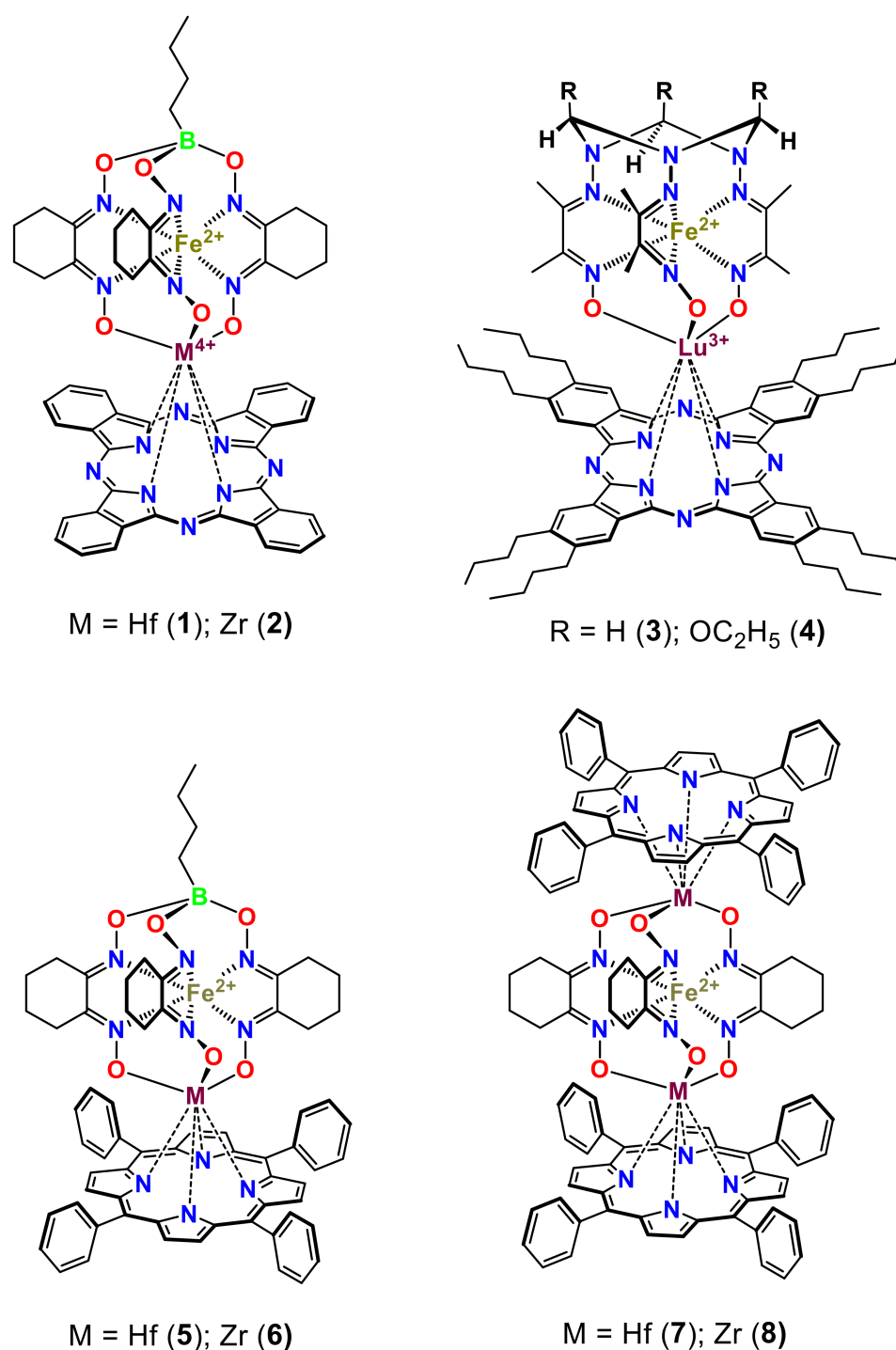
Keywords: clathrochelates; phthalocyanines; zirconium(IV); hafnium(IV); nickel(II); iron(II); spectroelectrochemistry; homogeneous catalysis; oxidation reactions; DFT calculations

1. Introduction

The covalent and coordination molecular assemblies with several electronically coupled metal centers are intensively studied [1–26] because of their prospective application in molecular electronics and light-harvesting (supra)molecular systems. Hybrid multicentered inorganic and organometallic transition metal arrays with relatively isolated π - and σ -electronic systems, which belong to different metal-centered frameworks, have received

a relatively little attention up to date. These polytopic compounds have proven to be potentially useful building blocks for the design of redox- and photoredox-driven molecular electronic devices and artificial photosynthetic systems with long-lived charge separation states [27–33]. In particular, this class of hybrid transition metal complexes includes zirconium(IV) and hafnium(IV), as well as lutetium(III) phthalocyaninate-capped iron(II) cage compounds **1–4** (so-called “phthalocyaninoclathrochelates”), first prepared about 15 years ago [34,35] (Scheme 1). Their molecules contain a phthalocyanine-centered extensive π -system that is coupled with a quasi-aromatic metal-encapsulating macrobicyclic framework. These compounds have been characterized by single crystal X-ray diffraction, spectroscopic and electrochemical methods. Detailed spectroelectrochemical study of the oxidation of these hybrid complexes is also reported [36]. By comparison of their redox potentials with those of the parent zirconium(IV) and hafnium(IV) phthalocyaninates, the first reversible oxidation and reduction waves in the corresponding cyclic voltammograms (CVs) were attributed to the apical phthalocyanine moiety [37,38]. The second quasi-reversible and the third irreversible anodic waves were assigned to the oxidation of the clathrochelate framework based on similarity to the oxidation processes observed in the case of the parent iron(II) clathrochelates [39,40]. To corroborate the experimental electrochemical assignments and the theoretical density functional theory (DFT) calculations, the spectroelectrochemical experiments for the hybrid complexes **1–3** (Scheme 1) have been conducted [36]. Upon oxidation at their first oxidation potential, the intensities of the initial phthalocyaninate-localized *Q*- and *B*-bands decreased, while three new absorption bands appeared in the UV–vis spectra of these complexes. The oxidation was accompanied by several isosbestic points, thus suggesting formation of the corresponding phthalocyaninate-centered mono- and di-cation-radicals [41]. In contrast, upon electrolysis at the second oxidation potential, all the phthalocyaninate-centered UV–vis bands characteristic for their monocationic-radical forms lost their intensities without appearance of new absorption bands. The initial neutral iron(II) phthalocyaninoclathrochelates **1–3** could not be regenerated from the corresponding doubly oxidized macropolycyclic dications. This fact indicates [36] that the doubly oxidized dications are not stable and degrade in solution. Further evidence provided the CV data [35], which revealed quasi-reversibility of the second oxidation process only at high scan rates.

The redox properties of hybrid di- and trinuclear Fe,Zr- and Fe,Hf-porphyrinoclathrochelates **5–8** shown in Scheme 1, which are formed by capping with Lewis-acidic M^{IV} TPP group(s), where M^{IV} is Zr^{4+} or Hf^{4+} cation and TPP^{2-} is 5,10,15,20-tetraporphyrinate dianion, were also investigated [42] by various electrochemical and spectroelectrochemical techniques. The results of the CV and differential pulse voltammetry (DPV) experiments suggested that, in the case of the monoporphyrinoclathrochelates **5** and **6**, three redox processes could be clearly identified. Two reversible oxidation waves were assigned to the $Fe^{2+/3+}$ and the $TPP^{1-/2-}$ clathrochelate- and porphyrinate-localized redox processes, respectively, while the cathodic wave was attributed [42] to the $TPP^{2-/3-}$ reduction. In the case of the iron(II) diporphyrinatoclathrochelates **7** and **8**, the $Fe^{2+/3+}$ redox process is substantially shifted to lower potentials due to a more electron-donating effect of its porphyrinate ligand fragment, as compared with that of the capping boron atom in the monoporphyrinato-clathrochelate analogs. The porphyrinate-centered oxidation of these tritopic complexes was observed [42] as two closely separated but clearly recognized redox waves. Analogously, two closely spaced porphyrinate-centered reduction waves have also been detected [42]. In general, the UV–vis spectra of these di- and tritopic hybrid complexes suggest a lack of any electronic communication between the clathrochelate and porphyrinate frameworks. The corresponding (spectro)electrochemical data [42] also indicated very weak, if any, long-range electronic coupling between two macroheterocyclic π -systems in the molecules of trinuclear iron(II) diporphyrinoclathrochelates.

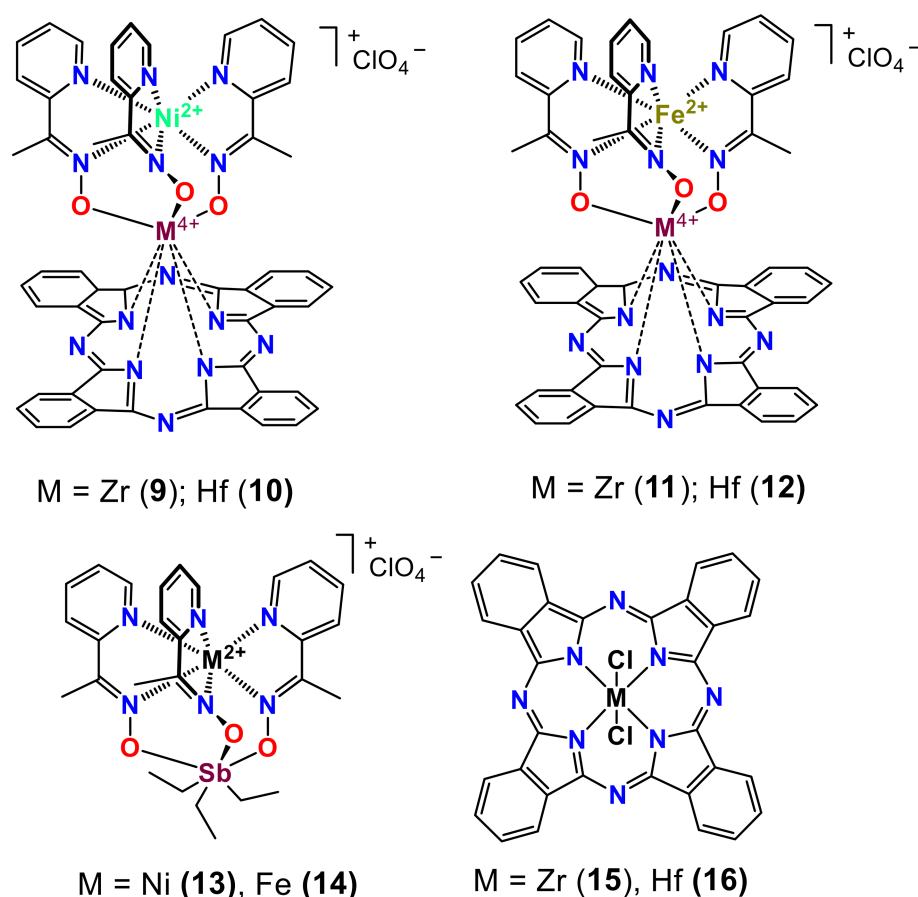


Scheme 1. Chemical drawings of the hybrid iron(II) phthalocyanino- and porphyrinoclathrochelates.

The phthalocyanine π -systems are known to possess photo- and electrochromic properties, as well as photocatalytic activity [43–45]. The phthalocyanine-based catalysts [46] can be easily obtained and possess very high chemical robustness even in harsh media. On the other hand, the designed *d*-metal clathrochelates were reported [47–49] to be useful for protein sensing or efficient electro- and (pre)catalysts for hydrogen and syngas (H₂ + CO) production. A series of the polyamine cobalt(III) cage complexes with tethered mercaptoethylamide terminated oligopeptide apical substituents, allowing for immobilization on a surface of the working gold electrode, was described [50] to be potent heterogeneous electrocatalysts in both the hydrogen evolution reaction (HER) and the oxygen reduction to hydrogen peroxide. Photodissociation of water was realized on rhodium-doped strontium

titanate photoelectrode surface modified by a cobalt(II) clathrochelate when using methanol as a sacrificial agent [51]. Polyamine cobalt(III) clathrochelates were reported to be active and robust homogeneous catalysts for the oxidation of styrene by H_2O_2 both in acetonitrile solution and in ionic liquid medium [52]. The mononuclear cobalt(II) cage complex of a heteroditopic N_5O_3 -macrobicyclic ligand was reported [53] to be an efficient catalyst for oxidation of a number of olefins and benzyl derivatives with molecular oxygen or 2-methylpropanal as the oxidants at room temperature and atmospheric pressure. Photoinduced catalytic oxygen production was realized in an aqueous acetonitrile in the presence of the mononuclear copper(II) cage complex with a fluorescent anthracene-containing polyamine macrobicyclic ligand as photocatalyst [54]. The unique water-stable iron(IV) clathrochelate [55] was discovered to catalyze the photochemical oxidation of water to dioxygen with high turnover frequency and with record turnover number, working at relatively low overpotential of this redox process [56].

Herein, we report on spectroelectrochemical studies of metal(IV) phthalocyaninate-capped iron(II) and nickel(II) tris-pyridineoximates along with their precursors shown in Scheme 2. In addition, the catalytic activity of 9–16 in homogeneous oxidation reactions of cyclohexane is also reported.



Scheme 2. Compounds 9–12 studied in this work (top) and their precursors 13–16 (lower panel).

2. Results and Discussion

Synthesis. The heterodinuclear hybrid complexes 9–12 (Scheme 2) were prepared in good yields (65–79%) by transmetalation of the monotriethylantimony(V)-capped nickel(II) and iron(II) tris-pyridineoximates 13 and 14 as the reactive complex precursors with zirconium(IV) and hafnium(IV) phthalocyaninates [$\text{Zr}(\text{Cl}_2)\text{Pc}$] (15) and [$\text{Hf}(\text{Cl}_2)\text{Pc}$] (16) (see Scheme 2) as the Lewis acids in methanol–dichloromethane solutions/suspensions at room temperature [57]. The identity of the compounds 9–16 was verified by IR spectra (Figures S1–S6) and ESI MS studies.

ESI mass spectrometry. Due to their cationic nature, the Ni- and Fe-containing compounds gave strong and clean single m/z -signals in the mass spectra. Their experimental masses and isotopic distributions corresponding to $[M]^+$ matched the theoretical values on the full MS level (Table 1 and Figure 1). The Zr- and Hf-containing Pc precursors **15** and **16** released the chlorides and were detected as methoxido adducts $[M - 2Cl + OCH_3]^+$ (Table 1), which stemmed from methanol used as the solvent.

Table 1. Experimental (m_{exp}) and theoretical (m_{theor}) m/z mass signals of the investigated compounds.

	Compound	Species Observed	m_{exp}	m_{theor}
Hetero-Bimetallic Coordination Complexes	9	$[M]^+$	1067.16	1067.15
	10	$[M]^+$	1155.18	1155.20
	11	$[M]^+$	1063.15	1063.16
	12	$[M]^+$	1153.17	1153.20
Synthetic Precursors	13	$[M]^+$	673.10	673.12
	14	$[M]^+$	669.11	669.12
	15	$[M - 2Cl + OCH_3]^+$	633.07	633.07
	16	$[M - 2Cl + OCH_3]^+$	723.12	723.11

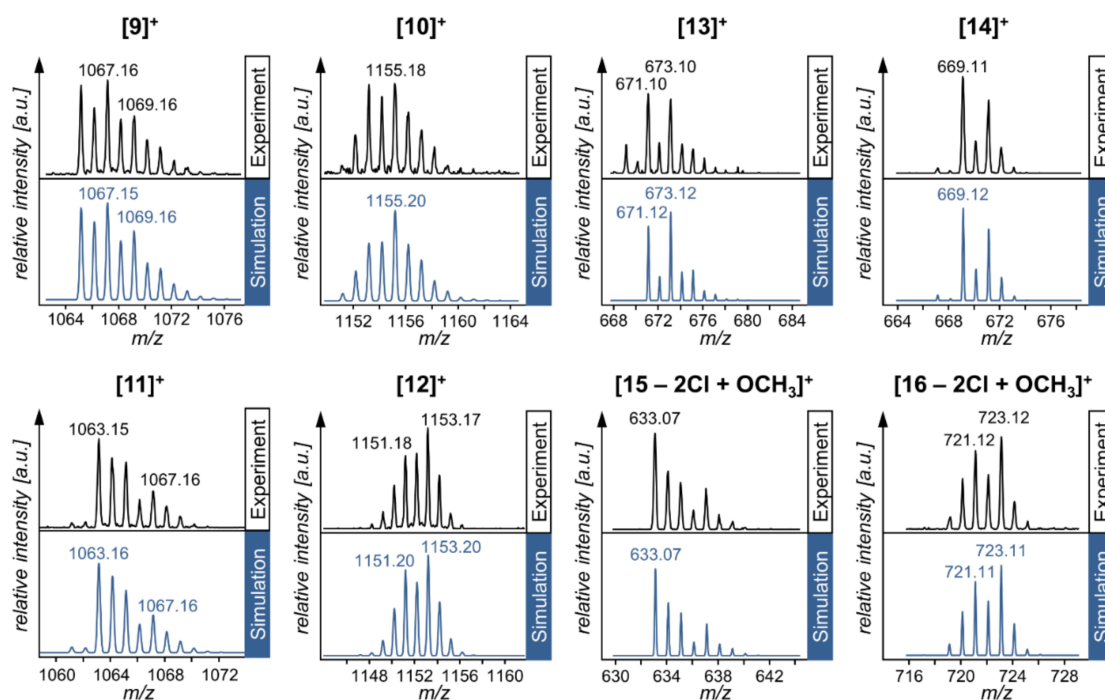


Figure 1. The experimental and theoretical isotopic distributions of the four investigated hetero-dimetallic complexes (**9–12**) and their synthetic precursors (**13–16**).

Each of the ionized compounds was then subjected to fragmentation experiments by collision-induced dissociation (CID). For this purpose, each precursor mass was selected and individually fragmented giving MS^2 spectra. The Ni-Sb precursor **13** mass did not yield fragment ions on the MS^2 level upon fragmentation. In contrast, the Fe-Sb precursor **14** showed ethyl group loss at the antimony, release of the chelating pyridineoximate ligand and oxidation (Figure S7).

Notably, the fragmentation spectra of **11** and **12** were similar, as were the respective fragment spectra of **9** and **10**. This indicates that the nickel(II) and iron(II) tris-

pyridineoximates have a stronger impact on the fragmentation pathways of **9–12** than the respective group 4 transition metals zirconium(IV) and hafnium(IV) (Figures S8 and S9).

The MS² spectra of the Fe-containing **11** and **12** (Figure S8) displayed characteristic fragments suggesting sequential release of the three pyridine ketimine moieties by cleaving the N–O bond and retaining O in the complex, i.e., $\Delta m = 118$. Furthermore, the fragment mass of 1082.2 of **12** might be indicative of FeO-release ($\Delta m = 71$). This was not observed for the iron analogue **11**.

Again, the nickel(II) complexes **9** and **10** yielded less fragments for interpretation. The fragmentation spectra of the nickel-containing **9** and **10** (Figure S9) showed a lower number of fragments, but the mass differences to the precursor ion suggested that the first pyridineoximate ligand was cleaved off intact, $\Delta m = 136$. Second, the $\Delta m = 116$ indicates the release of a pyridine ketimine ligand accompanied by redox changes on Ni, which was not observed for the Fe complexes. Release of the group 4 metals zirconium and hafnium was not observed. Then, MS³ experiments were performed for the bimetallic complexes by selecting a specific mass of each MS² spectrum, which was again subjected to fragmentation. The fragmentation energy of the MS³ level was slightly higher than at the MS² level. However, the MS³ level did not reveal significant new information about the investigated complexes (Figures S8 and S9).

Cyclic voltammetry, spectroelectrochemistry and DFT calculations. The cyclic voltammograms of complexes **9–12** in acetonitrile (ACN)/*n*-Bu₄NPF₆ (Figure S10) showed two fully reversible reduction waves and three oxidation events. Similar behavior was recently described for the same complexes in dichloromethane [57]. In the anodic part, the first two nearly reversible redox waves overlap, leading to the double peak shape. The third oxidation step is less reversible. Analogous redox response for all four investigated complexes indicates the ligand based redox locus. The reversibility and redox mechanism in the region of the first two reduction peaks for complex **9** (Ni–Zr) was further investigated by the in situ spectroelectrochemical UV-vis-NIR cyclic voltammetric experiments in ACN/*n*-Bu₄NPF₆ under argon atmosphere in a thin layer honeycomb spectroelectrochemical cell (Figure 2).

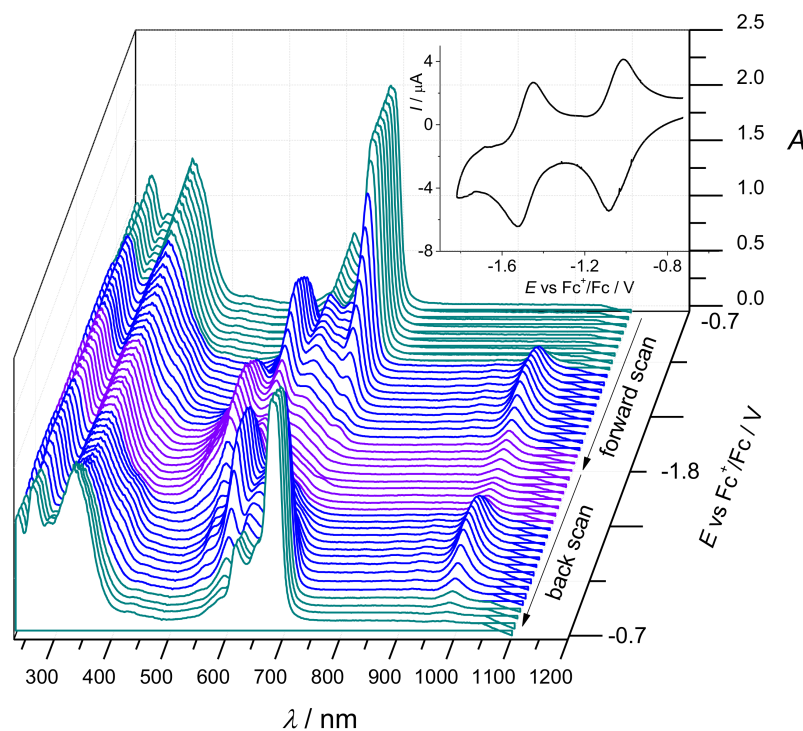


Figure 2. In situ UV-vis-NIR spectroelectrochemistry of complex **9** (Ni–Zr) in acetonitrile (ACN)/*n*-Bu₄NPF₆ in a thin layer honeycomb spectroelectrochemical cell: potential dependence of UV-vis-NIR spectra with corresponding cyclic voltammogram (scan rate $v = 10 \text{ mV s}^{-1}$).

Even by decreasing the scan rate to 10 mV s^{-1} , the cathodic reductions remain reversible and upon scan reversal the products formed upon reduction are fully re-oxidized back to the initial state. The recovery of the initial optical bands upon the voltammetric reverse scan confirms the electrochemical and chemical reversibility of the redox process at the first and the second reduction peak, respectively. It is worth noting that in the region of the first reduction peak, two new optical bands at 585 and 982 nm, with vibronic structure, emerged (Figure 3a).

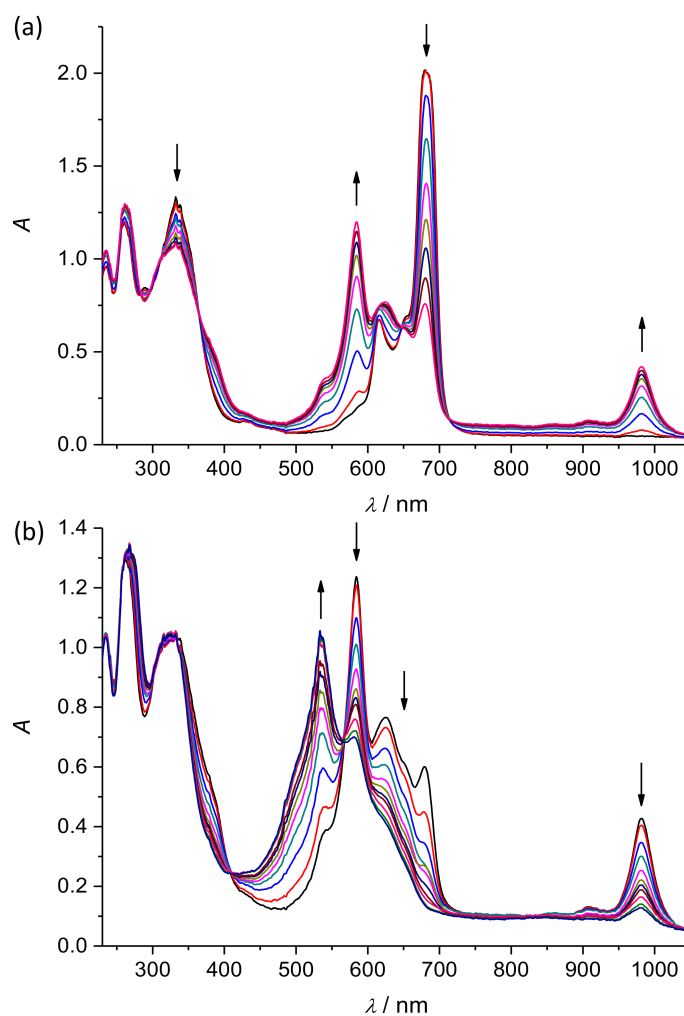


Figure 3. (a) Evolution of UV-vis-NIR spectra in 2D projection upon forward scan in the region of the first reduction peak for complex **9** (**Ni-Zr**) in ACN/*n*-Bu₄NPF₆ (black trace: -0.85 V , red trace: -0.90 V , blue trace: -0.95 V , dark cyan trace: -1.00 V , magenta trace: -1.05 V , dark yellow trace: -1.10 V , navy trace: -1.15 V , wine trace: -1.20 V , pink trace: -1.25 V , all vs. Fc^+/Fc); (b) evolution of UV-vis-NIR spectra in 2D projection upon forward scan in the region of the second reduction peak for **9** (black trace: -1.30 V , red trace: -1.35 V , blue trace: -1.40 V , dark cyan trace: -1.45 V , magenta trace: -1.50 V , dark yellow trace: -1.55 V , navy trace: -1.60 V , wine trace: -1.65 V , pink trace: -1.70 V , olive trace: -1.75 V , royal trace: -1.80 V , all vs. Fc^+/Fc).

In addition, a decrease in the intensity of the initial optical bands at 335 and 682 nm, characteristic of the phthalocyaninate unit, indicates that the reduction takes place mainly on this part of the complex. This reduction in the region of the first electron transfer was accompanied by several isosbestic points what is characteristic for the formation of the corresponding phthalocyaninate-centered radicals [41,58–60]. This was confirmed by in situ EPR spectroelectrochemistry where a single line EPR spectrum with a g -value of 2.0049 and a line width $\Delta H_{\text{pp}} = 7.7 \text{ G}$ appeared upon cathodic reduction at the first

reduction peak (see black trace in Figure 4), confirming large spin delocalization on the phthalocyaninate unit with an extensive π -system. Localization of the unpaired electron on the phthalocyaninate moiety has been further confirmed by the DFT calculations, as can be seen in the corresponding spin density distribution maps (Figure 5).

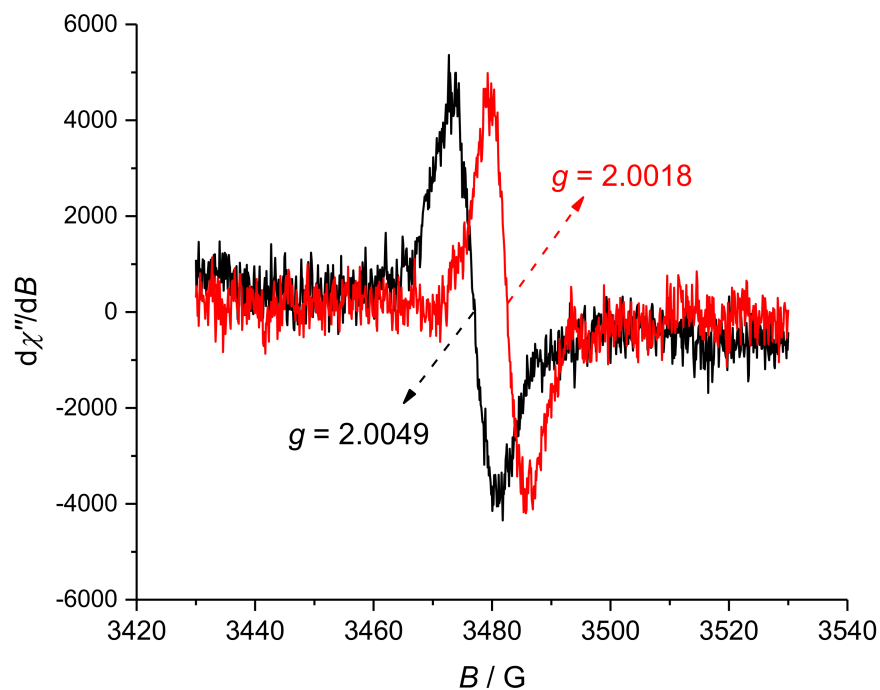


Figure 4. EPR spectra of the 1e-reduced **9** (Ni–Zr) (black trace) and 1e-oxidized **9** (Ni–Zr) (red trace) in ACN/*n*-Bu₄NPF₆.

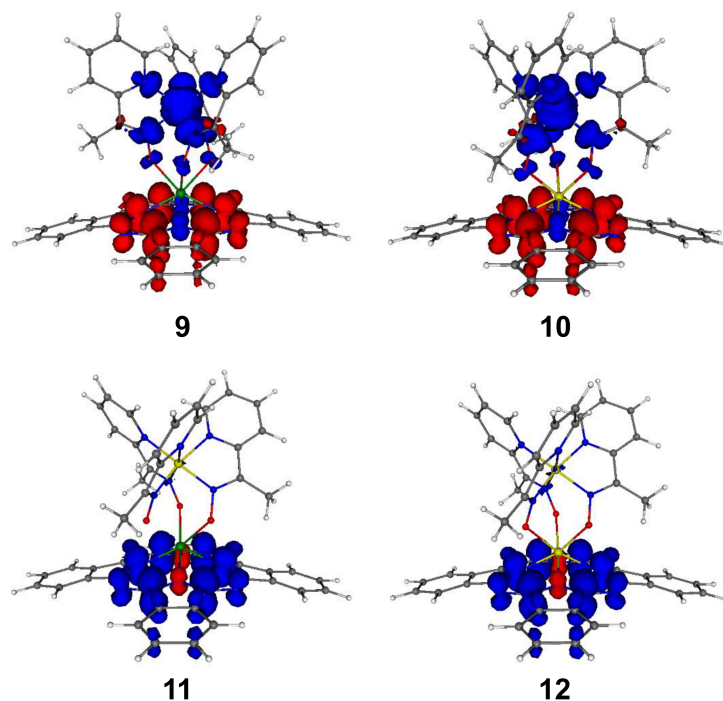


Figure 5. B3LYP/LanL2DZ-calculated spin density distributions in the 1e-reduced forms of the complexes **9**–**12**. The isovalue is set to ± 0.002 .

In the case of **11** and **12**, the spin density is localized exclusively on the phthalocyaninate moiety, while in the case of **9** and **10**, the spin density is found to be localized on the phthalocyaninate part as well as on the central atom (Ni) and in its vicinity (Figure 5).

At the second reduction peak, the bands of the 1e-reduced form at 585 and 982 nm decreased and a new band at 534 nm appeared. This can be attributed to the 2e-reduced form of phthalocyaninate moiety (Figure 3b). According to the DFT calculations, the triplet state is energetically preferred over the singlet state in these 2e-reduced forms of **9–12**, and the corresponding spin density distribution maps are displayed in Figure S11. A similar UV-vis-NIR spectroelectrochemical response was found for Fe–Zr analogue **11**, as shown in Figure S6a,b, and also for **12** (Ni–Zr) (Figure S12c,d)

In the region of the first oxidation double-peak, new optical bands at 544 and 852 nm were observed, as shown for **9** (Ni–Zr) in Figure 6, with a simultaneous decrease in the intensity of the initial optical bands at 335 and 682 nm, again indicating that the oxidation takes place mainly on the phthalocyanine part of the complex.

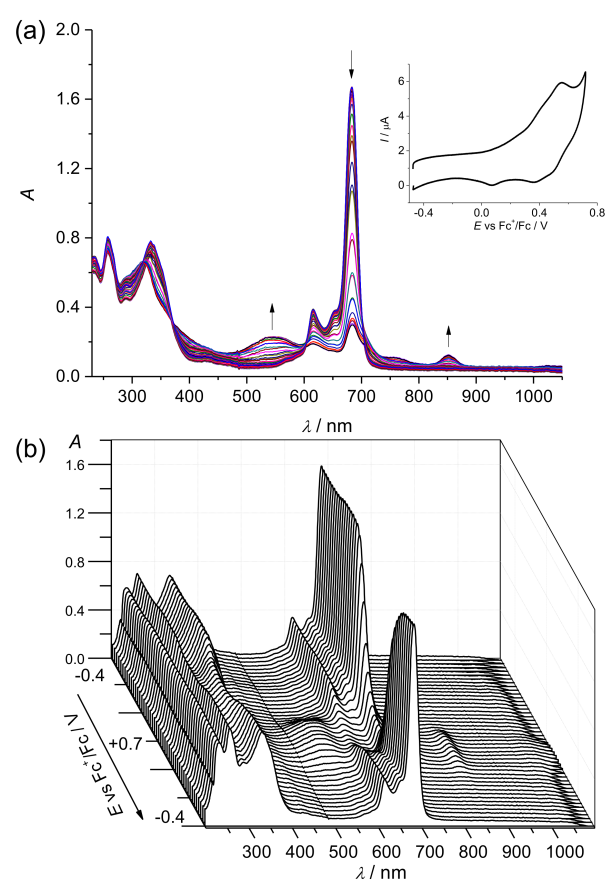


Figure 6. Evolution of UV-vis-NIR spectra in (a) 2D and (b) 3D projection upon cyclic voltammetry (see inset in (a)) in the region of the first oxidation double-peak for complex **9** (Ni–Zr) in ACN/*n*-Bu₄NPF₆ at scan rate $\nu = 10 \text{ mV s}^{-1}$.

Although the anodic oxidation is less reversible, as can be seen in the in situ cyclic voltammogram, it was possible to measure the EPR spectrum of the corresponding 1e-oxidized **9** (Ni–Zr) with a *g*-value of 2.0018, confirming even more delocalized spin density distribution in comparison to the 1e-reduced state (see red trace in Figure 4). Calculated spin density distribution maps of the oxidized forms of **9–12** (Figure S13) are very similar to the ones of their mono-reduced forms (Figure 5).

To confirm the suggested locus of the redox processes, the corresponding molecular precursors **13–16** (Scheme 2) were studied in detail by cyclic voltammetry (Figure S14) and spectroelectrochemistry. The electronic structure of 1e-oxidized and 1e-reduced states was

studied by electron paramagnetic resonance (EPR), UV–vis–near-IR spectroelectrochemistry, and density functional theory calculations.

One fully irreversible cathodic peak was found for metal(II) tris-pyridineoximate precursors **13** and **14** (Scheme 2) in ACN/*n*-Bu₄NPF₆ solutions (Figure S14a,b) at much more negative reduction potentials, as observed for the hybrid complexes (see Figure S10), providing evidence that the first two cathodic waves correspond to the reduction of Zr/Hf-phthalocyaninate units **15** and **16** (Scheme 2), which are reduced at much less negative reduction potentials (Figure S14c,d). Note that in the corresponding hybrids, much more reversible redox behavior was found compared to that of the precursors. So, the incorporation of metal(II) tris-pyridineoximates exerts a stabilization effect on the charged Zr/Hf-phthalocyaninate frameworks. Nevertheless, EPR spectroelectrochemistry confirmed the formation of phthalocyaninate centered both 1e-reduced and 1e-oxidized radicals, as shown in Figure S15 for precursor **15**. Interestingly, the corresponding 1e-reduced form of **15** exhibits the hyperfine splitting, while the 1e-oxidized form shows the single peak pattern, indicating larger spin delocalisation over the ligand, as confirmed by DFT calculations (see Figure S15, down).

The reversible anodic peak for Fe(II) tris-pyridineoximate **14** in ACN/*n*-Bu₄NPF₆ at +0.36 V vs. Fc⁺/Fc (Figure S14b) corresponds to the Fe²⁺/Fe³⁺ redox couple. During in situ UV-vis-NIR spectroelectrochemistry at 10 mV s^{−1} at the honeycomb platinum working electrode, a less reversible behavior was found, but upon reverse scan, a recovery of the initial optical band at 540 nm, characteristic for the Fe²⁺ state, was observed, indicating rather high stability of the Fe³⁺ form (Figure 7). This band was assigned to the Fe(d)—Ligand(π*) MLCT in the iron(II)-containing tris-pyridineoximate fragment [57], which indicates a noninnocent character of the ligand. This corresponds well to the shape of HOMO orbitals of **13** and **14** (see Figure S16 and Figure 8, respectively) and is in agreement with the noninnocent character of the tris-pyridineoximate moiety.

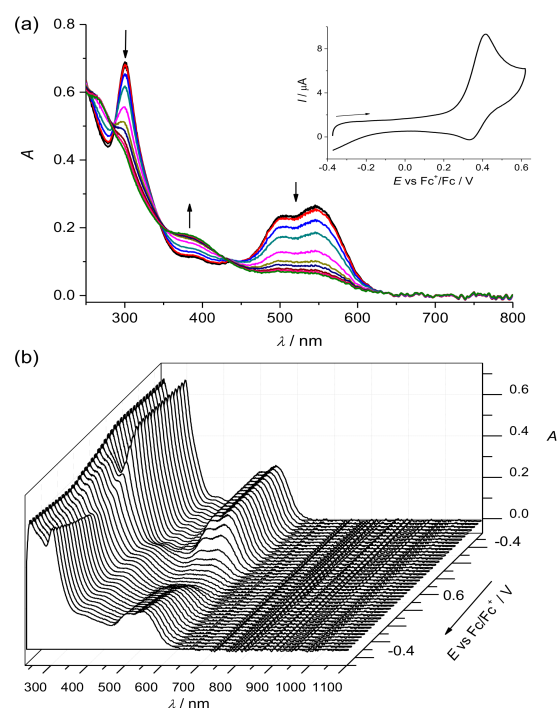


Figure 7. Evolution of UV-vis-NIR spectra in (a) 2D (forward scan, black trace: 0.15 V, red trace: 0.20 V, blue trace: 0.25 V, dark cyan trace: 0.30 V, magenta trace: 0.35 V, dark yellow trace: 0.40 V, navy trace: 0.45 V, wine trace: 0.50 V, pink trace: 0.55 V, olive trace: 0.60 V, all vs. Fc⁺/Fc) and (b) 3D projection during cyclic voltammetry (see the corresponding voltammogram in Inset of (a), scan rate 10 mV s^{−1}) of **14** in the region of the first oxidation peak in ACN/*n*-Bu₄NPF₆.

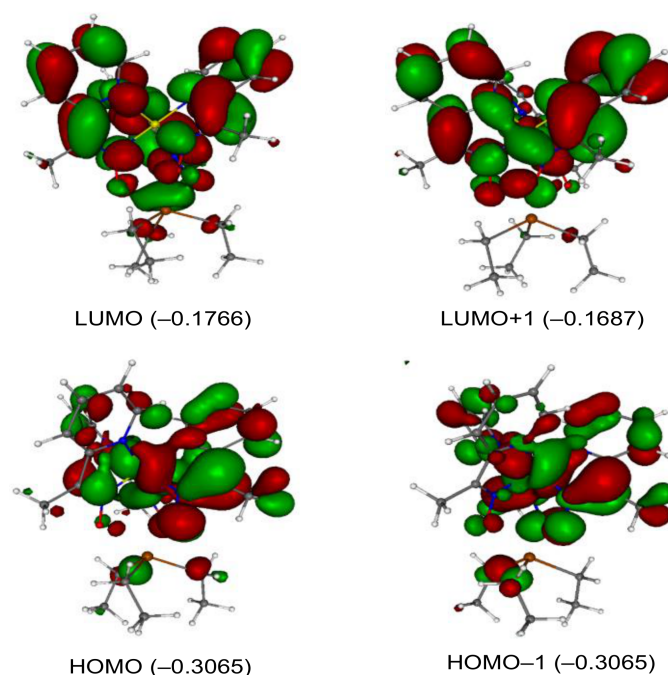


Figure 8. B3LYP/LanL2DZ HOMO-1, HOMO, LUMO, and LUMO+1 orbitals of the precursor **14**; the corresponding relative orbital energies in a.u. are given in parenthesis. The isovalue is set to ± 0.02 .

The Ni(II) tris-pyridineoximate precursor **13** in ACN/*n*-Bu₄NPF₆ showed an irreversible oxidation at $E_{pa} = 0.53$ V vs. Fc⁺/Fc that could be assigned to the Ni²⁺/Ni³⁺ redox couple. Analogous irreversible intense cathodic peaks at $E_{pc} = -1.93$ V vs. Fc⁺/Fc found for both M(II) tris-pyridineoximates **13** and **14** can be assigned to the 2e-reduction leading to the irreversible decomposition of the complexes, as evidenced by UV-vis-NIR spectroelectrochemistry for **14** (Figure S17).

Catalytic studies. The catalytic activity of dinuclear zirconium(IV) and hafnium(IV) phthalocyaninate-capped nickel(II) and iron(II) tris-pyridineoximate complexes **9–12** and their precursors **13–16** was tested for the peroxidative oxidation of cyclohexane as a model reaction. In fact, cyclohexane oxidation into cyclohexyl hydroperoxide and its deperoxidation into cyclohexanol and cyclohexanone are among the most important processes in the chemical industry, with the KA oil (cyclohexanone (K) + cyclohexanol (A)) mixture being the substrate for subsequent oxidation into adipic acid using nitric acid [61].

The catalytic experiments were initiated at room temperature and then by conventional thermal heating up to 60 °C, using an aqueous solution of tert-butyl hydroperoxide (THBP, 70%) as oxidizing agent (in view of its lower handling risk), and a low catalyst amount in ACN (see experimental).

The heterodinuclear hybrid complexes **9–12** exhibited some activity at room temperature (e.g., up to 9% KA oil yield for the Hf-Fe complex **12** after 6 h reaction), which was significantly enhanced by performing the oxidation reactions at 60 °C for the same time (6 h). Further increase in the temperature was avoided for safety reasons. The KA oil yields obtained under the optimized mild conditions are depicted in Figure 9.

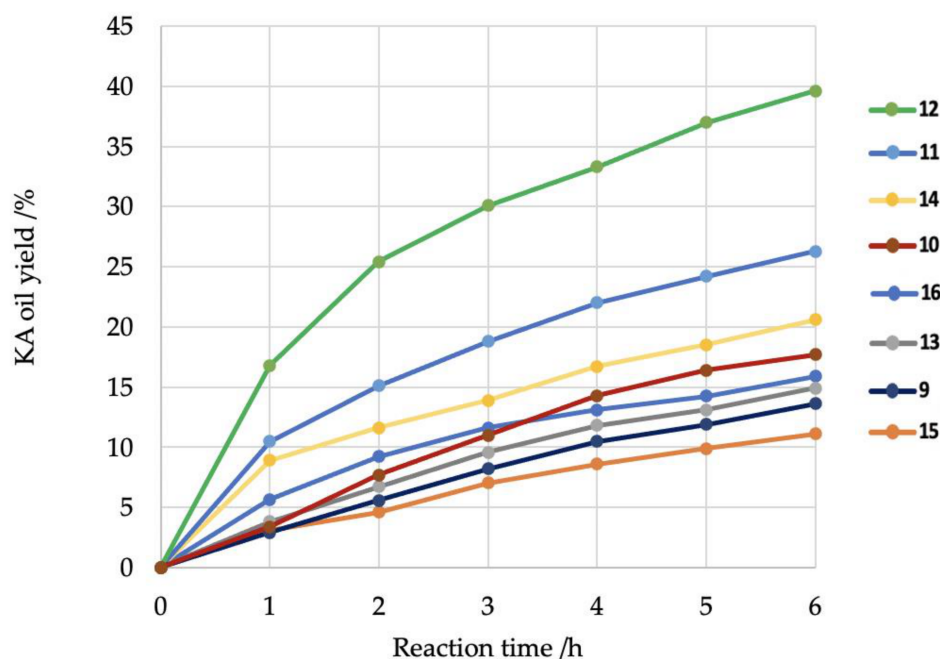


Figure 9. Effect of reaction time on the yield of KA oil obtained by oxidation of cyclohexane catalyzed by complexes 9–16. Optimized mild reaction conditions: catalyst (5 μmol), cyclohexane (2.5 mmol), tert-butyl hydroperoxide (TBHP) aq. sol. 70% (5.0 mmol), temperature = 60 $^{\circ}\text{C}$ (thermal heating) in ACN (3 mL). %Yield = moles of cyclohexanone + cyclohexanol per 100 mol of cyclohexane (gas chromatography (GC) yield after treatment with PPh_3).

The Hf-Fe complex **12** led to the highest KA oil yield (up to 36.9%) at 60 $^{\circ}\text{C}$ after 6 h reaction, suggesting a synergic effect on the catalytic activity of the heterodinuclear species. In fact, per se, the iron and hafnium complexes **14** and **16** yielded maxima of 20.6 and 15.9% of KA oil, respectively.

A similar synergism, although not so much pronounced, is observed for the Zr-Fe complex **11**, which exhibits a higher activity than those of the precursor iron (**14**) and zirconium (**15**) compounds (e.g., KA oil yields of 26.3, 20.6 and 11.1%, respectively, after 6 h at 60 $^{\circ}\text{C}$). However, eventual synergic effects are much less significant in the cases of the Hf-Ni (**10**) and Zr-Ni (**9**) dimetallic complexes. This suggests that the synergism is mainly based on the combination of the metals and not of the corresponding ligands.

The neutral compounds **15** and **16** (hence without the potentially dangerous perchlorate anion) were further tested for the MW-assisted oxidation of neat cyclohexane and, at the above optimized conditions (60 $^{\circ}\text{C}$), afforded up to 26% yield of cyclohexanol and cyclohexanone mixture (for complex **16**) after 3 h under irradiation (Figure 10). Thus, the microwave irradiation appears to enhance the catalytic activity of both **15** and **16**, leading to significantly higher KA oil yields (26.0 vs. 11.6% and 19.1 vs. 7.0%, respectively, for **16** and **15** after 3 h reaction) than those obtained under thermal heating (compare Figures 9 and 10). This is in accord with the previously observed behavior of other catalytic systems [62–64], where the use of MW irradiation provided a much more efficient synthetic method than conventional thermal heating. Due to the perchlorate counteranion of compounds 9–14, their catalytic performance comparison under MW conditions was avoided.

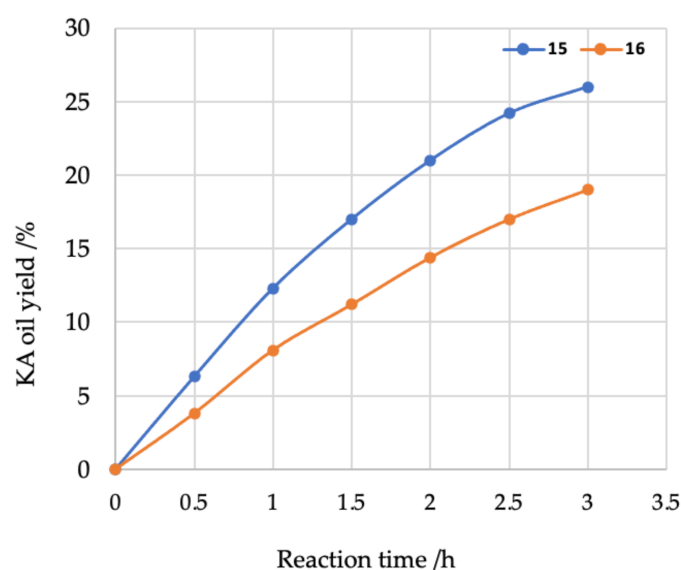


Figure 10. Effect of reaction time on the yield of KA oil obtained by microwave (MW)-assisted oxidation of neat cyclohexane catalyzed by complexes **15** and **16**. Reaction conditions: catalyst (5 μmol), cyclohexane (2.5 mmol), TBHP aq. sol. 70% (5.0 mmol), temperature = 60 $^{\circ}\text{C}$. %Yield = moles of cyclohexanone + cyclohexanol per 100 mol of cyclohexane (GC yield after treatment with PPh_3).

To date, the use of hafnium or zirconium as catalysts for the oxidation of cyclohexane is scarce. The first mention, in 1990, is a patented [65] process for the production of adipic acid by contacting cyclohexane with air at 80–160 $^{\circ}\text{C}$ and 2–100 bar in the presence of acetic acid, that used Zr and Hf co-catalysts (0.001–1000 atomic ratio Zr:Co, Hf:Co or (Zr+Hf):Co), making it possible to avoid the requirement for expensive halogen resistant construction materials. Two decades later, zirconium-porphyrinic iron-organic frameworks, with tetrakis(4-carboxyphenyl)porphyrin (TCPP), were applied by Zhou et al. [66], as catalysts for the cyclohexane oxidation to KA oil in the presence of TBHP (in decane) at 65 $^{\circ}\text{C}$, but no catalytic activity was observed for the Zr–porphyrinic (without iron) compound. The reactivity was attributed to the high-density of accessible active porphyrinic iron(III) centres within the porous framework. Transition metal exchanged alpha-zirconium phosphates, alpha-ZrP center dot M (where, M = Mn(II), Cu(II) or Fe(III)) were also tested [67] for the oxidation of cyclohexane in liquid phase with TBHP. The order of reactivity of alpha-ZrP center dot M was: alpha-ZrP center dot Mn(II) > alpha-ZrP center dot Cu(II) > alpha-ZrP center dot Fe(III). A maximum of 6% conversion and 100% selectivity for KA oil was observed with the alpha-ZrP center dot Mn(II)/TBHP system after 5 h of reaction, which could be recycled three times. Very recently [68], the magnetic $\text{ZrFe}_2\text{O}_4@\text{SiO}_2\text{-TCPP}$ nanocatalyst afforded a maximum of cyclohexanone and cyclohexanol products of 33.6 and 18.9%, respectively, with the advantage of being recovered by a magnetic field.

In the above cases, Zr is not the sole metal in the catalyst composition which also includes another transition metal with known catalytic activity in cyclohexane oxidation. Remarkably, in our study, besides the Zr and Hf heterobimetallic (9–12) complexes, we were also able to successfully use Zr and Hf monometallic neutral complexes (**15** and **16**) as efficient catalysts (yields up to 26% under MW irradiation, see Figure 10) for the selective oxidation of cyclohexane to the cyclohexanol and cyclohexanone mixture. Note that the current cyclohexane oxidation is a low-efficiency industrial process, with conversions lower than 10% to ensure a selectivity of 80% for the cyclohexanol/cyclohexanone mixture [69]. Thus, our catalytic outcomes represent a significant achievement in catalyst design for the industrially important cyclohexane oxidation.

The performed catalytic experiments support that cyclohexane oxidation catalyzed by our complexes proceeds through a mechanism of radical nature [70] where the catalyzed decomposition of *t*-BuOOH with formation of *t*-BuO and *t*-BuOO radicals is crucial for the

H-abstraction from cyclohexane, the beginning of its conversion through the radical pathway. Thus, the availability of reducible complexes (proved by the spectroelectrochemical and DFT studies) would be a key requirement for the oxidation to occur.

3. Materials and Methods

General procedures and measurements. All reactions were performed under inert atmosphere using the standard Schlenk techniques. All reagents were obtained from the commercial sources and used without additional purification. Hybrid complexes **9–12** and their precursors **13–16** were prepared as described previously [57]. The IR spectra of **9–14** (see Figures S1–S6) were in accord with previously reported data [57]. **Caution:** Complexes containing perchlorate should be handled with care.

Electrochemical, spectroelectrochemical and related EPR experiments. A Heka PG310USB (Lambrecht, Germany) potentiostat with a PotMaster 2.73 software package served as the potential control in cyclic voltammetric studies. Cyclic voltammetric experiments in acetonitrile (ACN) in the presence of *n*-Bu₄NPF₆ supporting electrolyte (puriss quality from Fluka) were performed under argon atmosphere using a three-electrode arrangement with platinum 1 mm disc working electrode (from Ionode, Tennyson, Australia), platinum wire as counter electrode, and silver wire as pseudo-reference electrode. Ferrocene (from Sigma-Aldrich, St. Louis, MO, USA) served as the internal potential standard. In situ ultraviolet-visible-near-infrared (UV-vis-NIR) spectroelectrochemical measurements were performed on a spectrometer Avantes (Model AvaSpec-2048 14-USB2, Apeldoorn, Netherlands) in the spectroelectrochemical cell kit (AKSTCKIT3) with the Pt-microstructured honeycomb working electrode, purchased from Pine Research Instrumentation (Durham, NC, USA). Halogen and deuterium lamps were used as light sources (Avantes, Model AvaLight-DH-S-BAL). The cell was positioned in the CUV-UV cuvette holder (Ocean Insight, Ostfildern, Germany). Optical spectra were processed using the AvaSoft 7.7 software package. Amperostatic electrochemical in situ EPR experiments were performed in acetonitrile solutions containing 0.5 mM of a given complex and 0.2 M of *n*-Bu₄NPF₆. The freshly prepared solutions were carefully purged with argon and inserted in a Varian electrolytic cell equipped with a large platinum mesh. The EPR spectra were measured in situ using an X-band EPR spectrometer EMX (Bruker, Karlsruhe, Germany) with 100 kHz field modulation.

Electrospray Ionization Mass Spectrometry. The compounds **9–12**, as well as their precursors **13–16**, were dissolved in methanol to a concentration of 1–5 μM and directly injected into the mass spectrometer. The compounds were analyzed intact and after fragmentation by collision-induced dissociation (CID) on MS² and MS³ levels. The analysis was performed on a Bruker AmaZon Speed ETD using trapControl Version 7.1 and Data Analysis 4.0 SP5 (Bruker Daltonics GmbH, Bremen, Germany). The compounds were infused at a flow rate of 3 μL min⁻¹. The data were acquired in the positive ion mode employing the following parameters: capillary voltage –4.5 kV, nebulizer 3 bar, dry gas 5 L min⁻¹, dry temperature 180 °C. The mass range was 100–2200. Fragmentation experiments by collision-induced dissociation (CID) were performed using amplification energies of 1.5–2.2 on the MS² level and MS³ experiments using amplification energies of 2.8–4.5. The low-level cut-off was 20% of the precursor mass by default.

Computational details. Geometry optimizations of the studied complexes (and their precursors) were performed at the B3LYP [71–74] /LanL2DZ [75,76] level of theory using the Gaussian09 program package [77]. The vibrational analysis was employed to confirm that the optimized geometries correspond to the energy minima (i.e., no imaginary vibration presented). Visualization of the optimized structures and the spin density distributions was performed using the Molekel software suite [78].

Catalytic studies. The catalytic tests were performed at room temperature or at 60 °C in a thermostated Pyrex round bottom flask and in open atmosphere, or under microwave (MW) irradiation. The MW experiments were undertaken in a focused Anton Paar Monowave 300 microwave incorporating a rotational system and an IR temperature detector (Anton

Paar GmbH, Graz, Austria), using a 10 mL capacity reaction tube with a 13 mm internal diameter. Complexes **9** to **16** were used. (**Caution:** the combination of perchlorates with many oxidizable substances may be explosive; dry perchlorates at elevated temperatures may be explosive!).

The peroxidative oxidation reactions were carried out as follows: 1–10 μmol of the complexes **9**–**16** were added to ACN (3.00 mL) with vigorous stirring, whereafter 2.50 mmol of cyclohexane (270 μL) and 5.00 mmol (690 μL) of tert-butyl hydroperoxide (TBHP, 70% aqueous solution) were added and the reaction solution was stirred for 0.5–3 h at the desired temperature (from room temperature to 60 $^{\circ}\text{C}$). Blank tests were performed in metal complex-free conditions.

The products analysis was performed as follows: 90 μL of cycloheptanone (internal standard), 10.00 mL of diethyl ether (to extract the substrate and the organic products from the reaction mixture) and an excess of triphenylphosphine were added. The obtained mixture was stirred for ca. 10 min and then a sample was taken from the organic phase and analysed by gas chromatography (GC).

GC measurements were carried out using a FISON Instruments GC 8000 series gas chromatograph with a flame ionization detector and a capillary column (DB-WAX, column length: 30 m; internal diameter: 0.32 mm) and the Jasco-Borwin v.1.50 software (Jasco, Tokyo, Japan). The temperature of injection was 240 $^{\circ}\text{C}$. The initial temperature was maintained at 100 $^{\circ}\text{C}$ for 1 min, then raised at 10 $^{\circ}\text{C}/\text{min}$ to 180 $^{\circ}\text{C}$ and held (at this temperature) for 1 min. Helium was used as the carrier gas. All products obtained from the catalytic oxidation reactions were identified by their retention times (confirmed with those of commercially available samples) and their quantification was attained by the internal standard method.

4. Conclusions

The ESI mass spectrometric study of **9**–**12** revealed pronounced similarity in fragmentation behavior of **9** and **10** as well as **11** and **12**. In particular, a sequential release of the three pyridine ketimine moieties was typical for the last two complexes.

The investigated hybrid molecular systems **9**–**12** exhibit quite rich redox activity both in the cathodic (two reversible reductions) and in the anodic region (two reversible and one quasi-reversible oxidations). EPR spectroelectrochemistry and DFT calculations indicate that the first reduction is due to the formation of phthalocyaninate-centered radical, while the second can be attributed to the 2e-reduced form of phthalocyaninate moiety. The dinuclear zirconium(IV) and hafnium(IV) phthalocyaninate-capped nickel(II) and iron(II) tris-pyridineoximate complexes **9**–**12** and their precursors **13**–**16** were found to catalyze the peroxidative oxidation of cyclohexane into cyclohexanol and cyclohexanone. The catalytic activity of **9**–**12** was low at room temperature, but increased significantly at 60 $^{\circ}\text{C}$. The Hf-Fe complex **12** showed the highest KA oil yield (up to 36.9%) after 6 h reaction time (Figure 9). The yield was higher than that achieved in the presence of iron and hafnium precursors **14** and **16** (20.6 and 15.9% of KA oil, respectively), implying a synergistic effect of the two metals in **12** on its catalytic activity. Less pronounced synergism was observed for other heterodinuclear complexes (**9**–**11**), but to a markedly lesser extent. Further temperature increase was avoided because of safety reasons. The synthesis of similar complexes to **9**–**12** with other than perchlorate counteranions and their testing at higher temperatures deserves attention. In this context, it should be stressed that the neutral compounds **15** and **16**, in which the counteranion is absent, have shown significantly higher KA oil yields in the MW-assisted oxidation of neat cyclohexane at 60 $^{\circ}\text{C}$ for 3 h (26.0 vs. 11.6 and 19.1 vs. 7.0%, respectively, for **16** and **15**) compared to those obtained by conventional thermal heating (Figure 10). The performed catalytic studies are in agreement with the mechanism of radical nature and availability of reducible complexes confirmed by spectroelectrochemical and theoretical DFT calculations.

Supplementary Materials: The following are available online, IR spectra Figure S1: IR spectrum of **9**, Figure S2: IR spectrum of **10**, Figure S3: IR spectrum of **11**, Figure S4: IR spectrum of **12**, Figure S5: IR spectrum of **13**, Figure S6: IR spectrum of **14**, the additional mass spectra with associated fragmentation experiments Figure S7: The full mass spectra (top) and the associated fragmentation experiment MS2 (bottom) upon isolation of the given precursor are shown for the synthetic precursor **14 (Fe–Sb)**. The corresponding Ni–Sb complex **13** did not yield interpretable fragmentation spectra, Figure S8: The full mass spectra (top) and their associated fragmentation experiments MS2 (middle) and MS3 (bottom) upon isolation of the given precursor are shown for **11 (Zr–Fe)** and **12 (Hf–Fe)**, Figure S9: The full mass spectra (top) and their associated fragmentation experiments MS2 (middle) and MS3 (bottom) upon isolation of the given precursor are shown for **9 (Zr–Ni)** and **10 (Hf–Ni)**, CVs for **9–12** Figure S10: Cyclic voltammograms for complexes (a) **9**, (b) **10**, (c) **11** and (d) **12**, in ACN/*n*-Bu₄NPF₆ (Pt-disc working electrode, scan rate 100 mV s⁻¹), B3LYP/LanL2DZ spin density distributions in the double-reduced forms of the **9–12** Figure S11: B3LYP/LanL2DZ Spin density distributions in double-reduced forms of complexes **9–12**. The isovalue is set to ±0.002. Energy differences between the singlet and triplet electronic states (ΔE_{S-T}) are 0.035, 0.034, 0.0035 and 0.0034 a.u. for complexes **9**, **10**, **11** and **12**, respectively. The in situ UV-vis-NIR spectra of **11** and **12** in the region of the first and the second reduction waves Figure S12: In situ UV-vis-NIR spectroelectrochemistry of complex **11 (Fe–Zr)** in the region of (a) the first and (b) the second cathodic peak, as well as of complex **12 (Fe–Hf)** in the region of (c) the first and (d) the second cathodic peak, all in ACN/*n*-Bu₄NPF₆ in a thin layer honeycomb spectroelectrochemical cell, B3LYP/LanL2DZ spin density distributions in the monooxidized forms of **9–12** Figure S13: B3LYP/LanL2DZ spin density distributions in 1e-oxidized forms of complexes **9–12**. The isovalue is set to ±0.002, CVs of **13–16** Figure S14: Cyclic voltammograms for the corresponding molecular precursors **13–16** of investigated hybrid Zr/Hf-phthalocyaninate-capped metal(II) tris-pyridineoximates **9–12** in ACN/*n*-Bu₄NPF₆ solutions (Pt-disc working electrode, scan rate 100 mV s⁻¹): (a) **13**, (b) **14**, (c) **15** and (d) **16**, EPR spectra and the spin density distributions for the monoreduced and monooxidized forms of the precursor **15** Figure S15: Top: EPR spectrum of 1e-reduced precursor **15** (black trace) and 1e-oxidized **15** (red trace) in ACN/*n*-Bu₄NPF₆. Bottom: B3LYP/LanL2DZ spin density distributions in 1e-reduced (left) and 1e-oxidized (right) precursor **15**. The isovalue is set to ±0.002, frontier orbitals of **13** Figure S16: B3LYP/LanL2DZ HOMO–1, HOMO, LUMO, and LUMO+1 orbitals of the precursor **13**, the corresponding relative orbital energies in a.u. are given in parenthesis. The isovalue is set to ±0.02, evolution of UV-vis-NIR spectra of the precursor **14** upon the corresponding CV experiment in the region of the first reduction wave Figure S17: Evolution of UV-vis-NIR spectra in (a) 2D (forward scan) and (b) 3D projection during cyclic voltammetry (see the corresponding voltammogram in Inset of (a), scan rate 10 mV s⁻¹) of **14** in the region of the first reduction peak in ACN/*n*-Bu₄NPF₆.

Author Contributions: Y.Z.V., S.V.D. and S.A.B. prepared the complexes and have written the introduction part, S.M.M.-M., D.G., D.S., C.-M.M., M.-A.L. performed and interpreted the ESI MS measurements, P.R. and D.D. performed electrochemical and spectroelectrochemical investigations, M.M. performed DFT calculations, A.J.L.P. and L.M.D.R.S.M. carried out the catalysis, V.B.A. supervised the project and was involved in writing the manuscript. All authors have read and agreed to the published version of the manuscript.

Funding: This work was supported by the European Commission H2020-MSCA-RISE-2017 Grant number, 778245, by the Slovak Grant Agencies APVV (contract Nos. APVV-15-0053, APVV-15-0079, APVV-19-0024 and DS-FR-19-0035) and VEGA (contracts No. 1/0139/20, 1/0718/19, 1/0504/20 and 1/0466/18), and by the Fundação para a Ciência e Tecnologia (FCT) and project UIDB/00100/2020 of Centro de Química Estrutural, Portugal. M.M. is grateful to the HPC center at the Slovak University of Technology in Bratislava, which is a part of the Slovak Infrastructure of High Performance Computing (SIVVP project, ITMS code 26230120002, funded by the European region development funds) for the computational time and resources made available. P.R. thanks the Ministry of Education, Science, Research and Sport of the Slovak Republic for funding within the scheme “Excellent research teams”. The synthesis of hybrid complexes and their precursor was supported by the Russian Science Foundation (grant 17-13-01468). Y.Z.V., S.V.D. and S.A.B. also thank the Russian Foundation for Basic Research (grants 18-29-23007 and 19-03-00357) for support of the spectral studies. The initial optical experiments were supported by INEOS RAS state assignment.

Data Availability Statement: Data available in a publicly accessible repository.

Conflicts of Interest: The authors declare no conflict of interest.

References

1. Heath, J.R.; Ratner, M.A. Molecular Electronics. *Physics Today* **2003**, *56*, 43–49. [[CrossRef](#)]
2. Nalwa, H.S. (Ed.) *Encyclopedia of Nanoscience and Nanotechnology*®; American Scientific Publ.: Stevenson Ranch, CA, USA, 2004.
3. Weiss, J. Supramolecular Approaches to Nano and Molecular Electronics. *Coord. Chem. Rev.* **2010**, *254*, 2247–2248. [[CrossRef](#)]
4. Lyshevski, S.E. (Ed.) Nano-and microscience, engineering, technology, and medicine series. In *Nano and Molecular Electronics Handbook*; CRC Press: Boca Raton, FL, USA, 2007.
5. Bayley, H. Holes with an Edge. *Nature* **2010**, *467*, 164–165. [[CrossRef](#)] [[PubMed](#)]
6. Giacalone, F.; Martín, N. New Concepts and Applications in the Macromolecular Chemistry of Fullerenes. *Adv. Mater.* **2010**, *22*, 4220–4248. [[CrossRef](#)] [[PubMed](#)]
7. Jurow, M.; Schuckman, A.E.; Batteas, J.D.; Drain, C.M. Porphyrins as Molecular Electronic Components of Functional Devices. *Coord. Chem. Rev.* **2010**, *254*, 2297–2310. [[CrossRef](#)]
8. Chung, A.; Deen, J.; Lee, J.-S.; Meyyappan, M. Nanoscale Memory Devices. *Nanotechnology* **2010**, *21*, 412001. [[CrossRef](#)]
9. Belosludov, R.V.; Farajian, A.A.; Kikuchi, Y.; Mizuseki, H.; Kawazoe, Y. Realization of Molecular Interconnection for Molecular Electronics: Theoretical Aspects. *Comput. Mater. Sci.* **2006**, *36*, 130–134. [[CrossRef](#)]
10. Belosludov, R.V.; Farajian, A.A.; Baba, H.; Mizuseki, H.; Kawazoe, Y. Electronic and Transport Properties of Doped Organic Molecules for Molecular Wire Applications. *Jpn. J. Appl. Phys.* **2005**, *44*, 2823–2825. [[CrossRef](#)]
11. Lee, S.U.; Belosludov, R.V.; Mizuseki, H.; Kawazoe, Y. Control of Electron Transport by Manipulating the Conjugated Framework. *J. Phys. Chem. C* **2007**, *111*, 15397–15403. [[CrossRef](#)]
12. Lehn, J.-M. *Supramolecular Chemistry: Concepts and Perspectives: A Personal Account. Built upon the George Fisher Baker Lectures in Chemistry at Cornell University [and] Lezioni Lincee, Accademia Nazionale Dei Lincei, Roma; VCH: Weinheim, Germany; New York, NY, USA, 1995.*
13. Balzani, V.; Juris, A.; Venturi, M.; Campagna, S.; Serroni, S. Luminescent and Redox-Active Polynuclear Transition Metal Complexes. *Chem. Rev.* **1996**, *96*, 759–834. [[CrossRef](#)]
14. Miller, J.S.; Epstein, A.J. Organische und metallorganische molekulare magnetische Materialien: Designer-Magnete. *Angew. Chem.* **1994**, *106*, 399–432. [[CrossRef](#)]
15. Barlow, S.; O'Hare, D. Metal–Metal Interactions in Linked Metallocenes. *Chem. Rev.* **1997**, *97*, 637–670. [[CrossRef](#)] [[PubMed](#)]
16. Kaim, W.; Lahiri, G.K. Unconventional Mixed-Valent Complexes of Ruthenium and Osmium. *Angew. Chem. Int. Ed.* **2007**, *46*, 1778–1796. [[CrossRef](#)] [[PubMed](#)]
17. Kaim, W.; Sarkar, B. Mixed Valency in Ruthenium Complexes—Coordinative Aspects. *Coord. Chem. Rev.* **2007**, *251*, 584–594. [[CrossRef](#)]
18. Venkatasubbaiah, K.; Doshi, A.; Nowik, I.; Herber, R.H.; Rheingold, A.L.; Jäkle, F. Examination of the Mixed-Valence State of the Doubly Boron-Bridged Diferrocene Cation [(FeCp)₂{μ-C10H6(BPh)₂}]⁺. *Chem. Eur. J.* **2008**, *14*, 444–458. [[CrossRef](#)] [[PubMed](#)]
19. Hadt, R.G.; Nemykin, V.N. Exploring the Ground and Excited State Potential Energy Landscapes of the Mixed-Valence Biferrocenium Complex. *Inorg. Chem.* **2009**, *48*, 3982–3992. [[CrossRef](#)]
20. Bucher, C.; Devillers, C.; Moutet, J.; Royal, G.; Saintaman, E. Ferrocene-Appended Porphyrins: Syntheses and Properties. *Coord. Chem. Rev.* **2009**, *253*, 21–36. [[CrossRef](#)]
21. Burrell, A.K.; Campbell, W.M.; Jameson, G.B.; Officer, D.L.; Boyd, P.D.W.; Zhao, Z.; Cocks, P.A.; Gordon, K.C. Bis(Ferrocenyl)Porphyrins. Compounds with Strong Long-Range Metal–Metal Coupling. *Chem. Commun.* **1999**, 637–638. [[CrossRef](#)]
22. Shoji, O.; Tanaka, H.; Kawai, T.; Kobuke, Y. Single Molecule Visualization of Coordination-Assembled Porphyrin Macrocycles Reinforced with Covalent Linkings. *J. Am. Chem. Soc.* **2005**, *127*, 8598–8599. [[CrossRef](#)]
23. Nemykin, V.N.; Rohde, G.T.; Barrett, C.D.; Hadt, R.G.; Bizzarri, C.; Galloni, P.; Floris, B.; Nowik, I.; Herber, R.H.; Marrani, A.G.; et al. Electron-Transfer Processes in Metal-Free Tetraferrocenylporphyrin. Understanding Internal Interactions To Access Mixed-Valence States Potentially Useful for Quantum Cellular Automata. *J. Am. Chem. Soc.* **2009**, *131*, 14969–14978. [[CrossRef](#)]
24. Solomon, E.I.; Sarangi, R.; Woertink, J.S.; Augustine, A.J.; Yoon, J.; Ghosh, S. O₂ and N₂ O Activation by Bi-, Tri-, and Tetranuclear Cu Clusters in Biology. *Acc. Chem. Res.* **2007**, *40*, 581–591. [[CrossRef](#)] [[PubMed](#)]
25. Xi, B.; Liu, I.P.-C.; Xu, G.-L.; Choudhuri, M.M.R.; DeRosa, M.C.; Crutchley, R.J.; Ren, T. Modulation of Electronic Couplings within Ru₂–Polyyne Frameworks. *J. Am. Chem. Soc.* **2011**, *133*, 15094–15104. [[CrossRef](#)] [[PubMed](#)]
26. Ishikawa, N.; Kaizu, Y. Synthetic, Spectroscopic and Theoretical Study of Novel Supramolecular Structures Composed of Lanthanide Phthalocyanine Double-Decker Complexes. *Coord. Chem. Rev.* **2002**, *226*, 93–101. [[CrossRef](#)]
27. Lent, C.S.; Isaksen, B.; Lieberman, M. Molecular Quantum-Dot Cellular Automata. *J. Am. Chem. Soc.* **2003**, *125*, 1056–1063. [[CrossRef](#)] [[PubMed](#)]
28. Steuerman, D.W.; Tseng, H.-R.; Peters, A.J.; Flood, A.H.; Jeppesen, J.O.; Nielsen, K.A.; Stoddart, J.F.; Heath, J.R. Molecular-Mechanical Switch-Based Solid-State Electrochromic Devices. *Angew. Chem. Int. Ed.* **2004**, *43*, 6486–6491. [[CrossRef](#)]
29. Leigh, D.A.; Morales, M.Á.F.; Pérez, E.M.; Wong, J.K.Y.; Saiz, C.G.; Slawin, A.M.Z.; Carmichael, A.J.; Haddleton, D.M.; Brouwer, A.M.; Buma, W.J.; et al. Patterning through Controlled Submolecular Motion: Rotaxane-Based Switches and Logic Gates That Function in Solution and Polymer Films. *Angew. Chem. Int. Ed.* **2005**, *44*, 3062–3067. [[CrossRef](#)]

30. Ohkubo, K.; Kotani, H.; Shao, J.; Ou, Z.; Kadish, K.M.; Li, G.; Pandey, R.K.; Fujitsuka, M.; Ito, O.; Imahori, H.; et al. Production of an Ultra-Long-Lived Charge-Separated State in a Zinc Chlorin–C60 Dyad by One-Step Photoinduced Electron Transfer. *Angew. Chem. Int. Ed.* **2004**, *43*, 853–856. [[CrossRef](#)]
31. Sutton, L.R.; Scheloske, M.; Pirner, K.S.; Hirsch, A.; Guldi, D.M.; Gisselbrecht, J.-P. Unexpected Change in Charge Transfer Behavior in a Cobalt(II) Porphyrin–Fullerene Conjugate That Stabilizes Radical Ion Pair States. *J. Am. Chem. Soc.* **2004**, *126*, 10370–10381. [[CrossRef](#)]
32. Baran, P.S.; Monaco, R.R.; Khan, A.U.; Schuster, D.I.; Wilson, S.R. Synthesis and Cation-Mediated Electronic Interactions of Two Novel Classes of Porphyrin–Fullerene Hybrids. *J. Am. Chem. Soc.* **1997**, *119*, 8363–8364. [[CrossRef](#)]
33. Zhang, T.-G.; Zhao, Y.; Asselberghs, I.; Persoons, A.; Clays, K.; Therien, M.J. Design, Synthesis, Linear, and Nonlinear Optical Properties of Conjugated (Porphinato)Zinc(II)-Based Donor–Acceptor Chromophores Featuring Nitrothiophenyl and Nitrooligothiophenyl Electron-Accepting Moieties. *J. Am. Chem. Soc.* **2005**, *127*, 9710–9720. [[CrossRef](#)]
34. Voloshin, Y.Z.; Varzatskii, O.A.; Tomilova, L.G.; Breusova, M.O.; Magdesieva, T.V.; Bubnov, Y.N.; Krämer, R. First Hybrid Oximehydrazonate Phthalocyaninoclathrochelates: The Synthesis and Properties of Lutetium Phthalocyanine-Capped Cage Iron(II) Complexes. *Polyhedron* **2007**, *26*, 2733–2740. [[CrossRef](#)]
35. Voloshin, Y.Z.; Varzatskii, O.A.; Korobko, S.V.; Chernii, V.Y.; Volkov, S.V.; Tomachynski, L.A.; Pehn’o, V.I.; Antipin, M.Y.; Starikova, Z.A. Ditopic Macropolycyclic Complexes: Synthesis of Hybrid Phthalocyaninoclathrochelates. *Inorg. Chem.* **2005**, *44*, 822–824. [[CrossRef](#)] [[PubMed](#)]
36. Sabin, J.R.; Varzatskii, O.A.; Voloshin, Y.Z.; Starikova, Z.A.; Novikov, V.V.; Nemykin, V.N. Insight into the Electronic Structure, Optical Properties, and Redox Behavior of the Hybrid Phthalocyaninoclathrochelates from Experimental and Density Functional Theory Approaches. *Inorg. Chem.* **2012**, *51*, 8362–8372. [[CrossRef](#)]
37. Kadish, K.M.; Morrison, M.M. Solvent and Substituent Effects on the Redox Reactions of Para-Substituted Tetraphenylporphyrin. *J. Am. Chem. Soc.* **1976**, *98*, 3326–3328. [[CrossRef](#)] [[PubMed](#)]
38. Kadish, K.M.; Smith, K.M.; Guilard, R. (Eds.) *The Porphyrin Handbook*; Academic Press: San Diego, CA, USA, 2000.
39. Voloshin, Y.Z.; Kostromina, N.A.; Krämer, R. (Eds.) *Clathrochelates: Synthesis, Structure, and Properties*, 1st ed.; Elsevier Science: Amsterdam, The Netherlands; Boston, MA, USA, 2002.
40. Voloshin, Y.Z.; Dolganov, A.V.; Varzatskii, O.A.; Bubnov, Y.N. Efficient Electrocatalytic Hydrogen Production from H⁺ Ions Using Specially Designed Boron-Capped Cobalt Clathrochelates. *Chem. Commun.* **2011**, *47*, 7737–7739. [[CrossRef](#)]
41. Ou, Z.; Zhan, R.; Tomachynski, L.A.; Chernii, V.Y.; Kadish, K.M. Electrochemistry and Spectroelectrochemistry of Zirconium(IV) and Hafnium(IV) Phthalocyanines with β -Diketone Axial Ligands in Nonaqueous Media. *Macroheterocycles* **2011**, *5*, 164–170. [[CrossRef](#)]
42. Dudkin, S.V.; Erickson, N.R.; Vologzhanina, A.V.; Novikov, V.V.; Rhoda, H.M.; Holstrom, C.D.; Zatsikha, Y.V.; Yusubov, M.S.; Voloshin, Y.Z.; Nemykin, V.N. Preparation, X-Ray Structures, Spectroscopic, and Redox Properties of Di- and Trinuclear Iron–Zirconium and Iron–Hafnium Porphyrinoclathrochelates. *Inorg. Chem.* **2016**, *55*, 11867–11882. [[CrossRef](#)]
43. D’Souza, F.; Ito, O. Photosensitized Electron Transfer Processes of Nanocarbons Applicable to Solar Cells. *Chem. Soc. Rev.* **2012**, *41*, 86–96. [[CrossRef](#)]
44. Wróbel, D.; Graja, A. Photoinduced Electron Transfer Processes in Fullerene–Organic Chromophore Systems. *Coord. Chem. Rev.* **2011**, *255*, 2555–2577. [[CrossRef](#)]
45. Zagal, J.H.; Griveau, S.; Silva, J.F.; Nyokong, T.; Bedioui, F. Metallophthalocyanine-Based Molecular Materials as Catalysts for Electrochemical Reactions. *Coord. Chem. Rev.* **2010**, *254*, 2755–2791. [[CrossRef](#)]
46. Sorokin, A.B. Phthalocyanine Metal Complexes in Catalysis. *Chem. Rev.* **2013**, *113*, 8152–8191. [[CrossRef](#)] [[PubMed](#)]
47. Losytskyy, M.; Chornenka, N.; Vakarov, S.; Meier-Menches, S.M.; Gerner, C.; Potocki, S.; Arion, V.B.; Gumienna-Kontecka, E.; Voloshin, Y.; Kovalska, V. Sensing of Proteins by ICD Response of Iron(II) Clathrochelates Functionalized by Carboxyalkylsulfide Groups. *Biomolecules* **2020**, *10*, 1602. [[CrossRef](#)] [[PubMed](#)]
48. Voloshin, Y.; Belaya, I.; Krämer, R. *Cage Metal. Complexes: Clathrochelates Revisited*, 1st ed.; Springer International Publishing Imprint: Cham, Germany, 2017.
49. Voloshin, Y.Z.; Buznik, V.M.; Dedov, A.G. New Types of the Hybrid Functional Materials Based on Cage Metal Complexes for (Electro) Catalytic Hydrogen Production. *Pure Appl. Chem.* **2020**, *92*, 1159–1174. [[CrossRef](#)]
50. Harrowfield, J.M.; Koutsantonis, G.A.; Kraatz, H.-B.; Nealon, G.L.; Orłowski, G.A.; Skelton, B.W.; White, A.H. Cages on Surfaces: Thiol Functionalisation of Co(III) Sarcophagine Complexes. *Eur. J. Inorg. Chem.* **2007**, 263–278. [[CrossRef](#)]
51. Antuch, M.; Millet, P.; Iwase, A.; Kudo, A.; Grigoriev, S.A.; Voloshin, Y.Z. Characterization of Rh: SrTiO₃ Photoelectrodes Surface-Modified with a Cobalt Clathrochelate and Their Application to the Hydrogen Evolution Reaction. *Electrochim. Acta* **2017**, *258*, 255–265. [[CrossRef](#)]
52. Ribeiro, S.; Cunha-Silva, L.; Balula, S.S.; Gago, S. Cobalt(III) Sepulchrate Complexes: Application as Sustainable Oxidative Catalysts. *New J. Chem.* **2014**, *38*, 2500–2507. [[CrossRef](#)]
53. Chand, D.K.; Bharadwaj, P.K. A Cobalt(II) Cryptate of a Heteroditopic Cryptand L as an Efficient Oxygenation Catalyst of Organic Substrates Using Molecular Oxygen and 2-Methylpropanal. *Inorg. Chem.* **1997**, *36*, 5658–5660. [[CrossRef](#)]
54. Hao, H.-G.; Zheng, X.-D.; Lu, T.-B. Photoinduced Catalytic Reaction by a Fluorescent Active Cryptand Containing an Anthracene Fragment. *Angew. Chem. Int. Ed.* **2010**, *49*, 8148–8151. [[CrossRef](#)]

55. Tomyň, S.; Shylin, S.I.; Bykov, D.; Ksenofontov, V.; Gumienna-Kontecka, E.; Bon, V.; Fritsky, I.O. Indefinitely Stable Iron(IV) Cage Complexes Formed in Water by Air Oxidation. *Nat. Commun.* **2017**, *8*, 14099. [[CrossRef](#)]
56. Shylin, S.I.; Pavliuk, M.V.; D'Amario, L.; Mamedov, F.; Sá, J.; Berggren, G.; Fritsky, I.O. Efficient Visible Light-Driven Water Oxidation Catalysed by an Iron(IV) Clathrochelate Complex. *Chem. Commun.* **2019**, *55*, 3335–3338. [[CrossRef](#)]
57. Dudkin, S.V.; Belov, A.S.; Nelyubina, Y.V.; Savchuk, A.V.; Pavlov, A.A.; Novikov, V.V.; Voloshin, Y.Z. Synthesis, X-ray Structure and Electrochemical Properties of Hybrid Binuclear Metallophthalocyaninate-Capped Tris-Pyridineoximates. *New J. Chem.* **2017**, *41*, 3251–3259. [[CrossRef](#)]
58. Nyokong, T.; Gasyna, Z.; Stillman, M.J. Phthalocyanine.Pi.-Cation-Radical Species: Photochemical and Electrochemical Preparation of [ZnPc(-1).+ in Solution. *Inorg. Chem.* **1987**, *26*, 548–553. [[CrossRef](#)]
59. Nyokong, T.; Gasyna, Z.; Stillman, M.J. Analysis of the Absorption and Magnetic Circular Dichroism Spectra of Zinc Phthalocyanine and the.Pi.-Cation-Radical Species [ZnPc(1-)].Cntdot.+ . *Inorg. Chem.* **1987**, *26*, 1087–1095. [[CrossRef](#)]
60. Nemykin, V.N.; Chernii, V.Y.; Volkov, S.V. Synthesis and Characterization of New Mixed-Ligand Lanthanide–Phthalocyanine Cation Radical Complexes. *J. Chem. Soc., Dalton Trans.* **1998**, 2995–3000. [[CrossRef](#)]
61. Hobbs, C.C. Hydrocarbon Oxidation. In *Kirk-Othmer Encyclopedia of Chemical Technology*; John Wiley & Sons, Inc.: New York, NY, USA, 1995; Volume 13.
62. Timokhin, I.; Pettinari, C.; Marchetti, F.; Pettinari, R.; Condello, F.; Galli, S.; Alegria, E.C.B.A.; Martins, L.M.D.R.S.; Pombeiro, A.J.L. Novel Coordination Polymers with (Pyrazolato)-Based Tectons: Catalytic Activity in the Peroxidative Oxidation of Alcohols and Cyclohexane. *Cryst. Growth Des.* **2015**, *15*, 2303–2317. [[CrossRef](#)]
63. Sutradhar, M.; Martins, L.M.D.R.S.; Guedes da Silva, M.F.C.; Pombeiro, A.J.L. Oxidovanadium Complexes with Tridentate Aroylhydrazone as Catalyst Precursors for Solvent-Free Microwave-Assisted Oxidation of Alcohols. *Appl. Catal. A Gen.* **2015**, *493*, 50–57. [[CrossRef](#)]
64. Martins, L.M.D.R.S.; Ribeiro, A.P.C.; Carabineiro, S.A.C.; Figueiredo, J.L.; Pombeiro, A.J.L. Highly Efficient and Reusable CNT Supported Iron(II) Catalyst for Microwave Assisted Alcohol Oxidation. *Dalton Trans.* **2016**, *45*, 6816–6819. [[CrossRef](#)] [[PubMed](#)]
65. Steinmetz, G.R.; Lafferty, N.L.; Sumner, C.E. Catalyst Contg. Cobalt, Zirconium and Opt. Hafnium for Adipic Acid—Prepd. by Air Oxidn. of Cyclohexane in Presence of Acetic and per-Acetic Acids Affords High Yields and Selectivity. U.S. Patent US4902827-A, 1990.
66. Feng, D.; Jiang, H.-L.; Chen, Y.-P.; Gu, Z.-Y.; Wei, Z.; Zhou, H.-C. Metal–Organic Frameworks Based on Previously Unknown Zr₈/Hf₈ Cubic Clusters. *Inorg. Chem.* **2013**, *52*, 12661–12667. [[CrossRef](#)]
67. Khare, S.; Shrivastava, P.; Chokhare, R.; Kirar, J.S.; Parashar, S. Catalytic Liquid Phase Oxidation of Cyclohexane with Tert-Butylhydroperoxide over Transition Metal Exchanged Alpha-Zirconium Phosphate. *Ind. J. Chem., Sect. A* **2018**, *57A*, 424–434.
68. Khosravi, H.B.; Rahimi, R.; Rabhani, M.; Maleki, A.; Mollahosseini, A. Design, Facile Synthesis and Characterization of Porphyrin-Zirconium-Ferrite@SiO₂ Core-Shell and Catalytic Application in Cyclohexane Oxidation. *Silicon* **2020**. [[CrossRef](#)]
69. *Ullmann's Encyclopedia of Industrial Chemistry*, 6th ed.; Wiley-VCH: Weinheim, Germany, 2016.
70. Shul'pin, G. Hydrocarbon Oxygenations with Peroxides Catalyzed by Metal Compounds. *MROC* **2009**, *6*, 95–104. [[CrossRef](#)]
71. Becke, A.D. Density-Functional Exchange-Energy Approximation with Correct Asymptotic Behavior. *Phys. Rev. A* **1988**, *38*, 3098–3100. [[CrossRef](#)] [[PubMed](#)]
72. Lee, C.; Yang, W.; Parr, R.G. Development of the Colle-Salvetti Correlation-Energy Formula into a Functional of the Electron Density. *Phys. Rev. B* **1988**, *37*, 785–789. [[CrossRef](#)] [[PubMed](#)]
73. Vosko, S.H.; Wilk, L.; Nusair, M. Accurate Spin-Dependent Electron Liquid Correlation Energies for Local Spin Density Calculations: A Critical Analysis. *Can. J. Phys.* **1980**, *58*, 1200–1211. [[CrossRef](#)]
74. Becke, A.D. Density-functional Thermochemistry. III. The Role of Exact Exchange. *J. Chem. Phys.* **1993**, *98*, 5648–5652. [[CrossRef](#)]
75. Hay, P.J.; Wadt, W.R. *Ab Initio* Effective Core Potentials for Molecular Calculations. Potentials for K to Au Including the Outermost Core Orbitals. *J. Chem. Phys.* **1985**, *82*, 299–310. [[CrossRef](#)]
76. *Methods of Electronic Structure Theory*, 1977th ed.; Schaefer, H.F. (Ed.) Springer: Berlin/Heidelberg, Germany, 2013.
77. Frisch, M.J.; Trucks, G.W.; Schlegel, H.B.; Scuseria, G.E.; Robb, M.A.; Cheeseman, J.R.; Scalmani, G.; Barone, V.; Mennucci, B.; Petersson, G.A.; et al. *Fox. Gaussian 09, Revision E.01*; Gaussian, Inc.: Wallingford, CT, USA, 2009.
78. Flükiger, P.; Lüthi, H.P.; Portmann, S.; Weber, J. *MOLEKEL 4.3*; Swiss Center for Scientific Computing: Manno, Switzerland, 2000.